Supporting Information

Synergistic heterojunction engineering and photothermal 3D confinement effect for enhanced photocatalytic overall water splitting

Jun Hou[a1], Junjie Wang[a1], Dongfang Hou*[a,b], Houfeng Zhang[a], Bojing Sun[a,b], Xiuqing Qiao[a,b], Huijuan Ma[b], Dongsheng Li*[a,b]

[a] College of Materials and Chemical Engineering, Key Laboratory of Inorganic Nonmetallic Crystalline and Energy Conversion Materials, China Three Gorges University,Yichang, 443002, China

[b] Hubei Three Gorges Laboratory,Yichang, 443007, China

*Corresponding author. dfhouok@126.com (D. Hou); lidongsheng1@126.com (D.-S. Li)

1. Synthesis of pure WO_2

According to the previous report[1], commercial WO_3 (200 mg) was dispersed in 15 mL of ethylenediamine under vigorous stirring for 40 minutes in a 50 mL Teflon-lined stainless-steel autoclave. Subsequently, the system was treated at 180 °C for 10 hours and cooled down to room temperature spontaneously. The resulting products, referred to as WO_x-precursors, were collected by centrifugation, washed three times with water and ethanol respectively, and dried under vacuum at 60 °C overnight. Then the WO_x-precursors underwent heating in an N_2 flow using a three-stage heating ramp: starting from room temperature to 350 °C at a rate of 5 °C min^{-1}, then increasing to 700 °C at a rate of 1 °C min^{-1} and holding that temperature for 5 hours. Finally, the product was naturally cooled to room temperature to obtain pure WO_2.

2. Characterization

The phase and crystal structures of the samples were determined by power X-ray diffraction (XRD; Ultima IV, Japan) with Cu Kα radiation (λ=1.5418 Å) in the diffraction range from 5°-80°. The micro-structure and morphology of as-prepare photocatalyst were recorded on a JEOL-JSM-7500F field emission scanning electron microscopy (FESEM）. The surface morphology and elemental composition were examined by transmission electron microscopy (TEM, Tecnai G2 F20 S-TWIN, accelerating voltage 200 kV) and energy-dispersive X-ray (EDX) spectroscopy. The surface chemical valance of the samples were analyzed through X-ray photoelectron spectroscopy (XPS, Al-Kα) on an ESCALAB 250 equipment. The N_2 adsorption-desorption isotherms of the samples were obtained by a Belsorp-max system. The specific surface area and pore size distribution were calculated through Brunauer–Emmett–Teller (BET) and Barrett–Joyner–Halenda (BJH) analysis, respectively. The UV-vis diffuse reflectance spectroscopy (DRS) was carried out with the ultraviolet-visible spectrophotometer (PerkinElmer USA) with $BaSO_4$ as a reflectance standard. The ptotoluminescence (PL) spectra and time-resolved spectrum were acquired by (PerkinElmer USA) instrument. A three-electrode system was used to obtain the electrochemical and photoelectrochemical information at CHI 660 electrochemical workstation. Infrared thermal imaging technology was used to evaluate the photothermal effect of photocatalysts under continuous irradiation with different light source (AM 1.5G simulated solar, NIR light (> 700 nm) and visible light (> 420 nm)) by a Testo 865 thermal imager at room room temperature (17 ℃). Surface potential distribution under dark and simulated sunlight were measured by the Kelvin probe force microscopy measurements (KPFM) at scanning probe microscope (SPM) system (Bruker Dimension

icon, Germany). Thermal diffusivity of the samples were measured by a laser flash technique using a Netzsch LFA457 thermal constant analyzer. Each circular sample is 1.5 mm in thickness and all the samples were sprayed by graphite solvent before the heating process to make sure the same black color is detected by the infrared thermal imaging spectrometer to reduce the error brought by the difference of thermal emissivity.

3. Photocatalytic activity tests

Photocatalytic tests were performed in a 200 mL quartz reactor with an online photocatalytic analysis system (Labsolar-6A, Beijing Perfectlight) at ambient temperature. Typically, 50 mg of photocatalyst was dispersed in 80 mL of deionized water. Prior to the reaction, the quartz chamber was purged with Ar atmosphere for 20 minutes to eliminate gas from the system. Subsequently, the reactor was positioned under a 300 W xenon lamp light source (PLS-SCE300D/300DUV, Beijing Perfectlight). Gas evolution was analyzed by an online gas chromatograph (GC9790II, FULI INSTRUMENTS), while 20 mL of argon was passed in to facilitate the detection of the subtle gas evolution. The apparent quantum efficiency (AQE) was performed using the same system under the illumination of a 300 W Xe lamp with several band pass filters. The AQE was calculated according to the following Eq. (S1):

$$AQE = \frac{2 \times the\ number\ of\ evolved\ H_2\ molecules}{the\ number\ of\ incident\ photons} \times 100\% \quad \text{(S1)}$$

4. Photoelectrochemical measurements

The photoelectrochemical measurements were investigated using an electrochemical workstation (CHI 660E, Chenhua, Shanghai, China) in the standard three-electrode configuration with FTO conductive glass as photoanodes, an saturated calomel electrode as reference electrode, Pt filament as the counter electrode in 0.5 M Na_2SO_4 solution. More details, the work electrode was prepared as follows: 4 mg as-prepared photocatalyst was dispersed in a mixed aqueous solution containing 700 μL DI water, 200 μL ethanol and 100 μL Nafion solution, then the mixture was sonicated for 30 min. Subsequently, 60 μL of the above suspension was applied onto the FTO conductive glass and dried at 60 °C overnight. The transient photocurrent response (TPR) was obtained using a 300W Xe lamp with a 420 nm cut-off filter. Electrochemical impedance spectroscopy (EIS) was measured in the frequency range of 0.01 Hz to 1k Hz. Mott-Schottky (M-S) curves were conducted at different frequencies.

5. Calculation of photothermal conversion efficiency

The internal photothermal conversion efficiency (η) of the WCM-10% heterostructure using the following Eq. (S2) [2,3]:

$$\eta = \frac{hs(T_{max} - T_0) - Q_{dis}}{I_{in}} \quad \text{(S2)}$$

where h is the heat transfer coefficient, and s is the surface area of the heat dissipation material. T_{max} is the highest temperature of the solution and T_0 is room temperature. Q_{dis} represents the heat from light absorbed by the quartz sample cell itself using a cuvette containing pure water. I_{in} is the energy power absorbed by WCM-10% heterostructure, which was determined by measuring the incident and transmitted light through WCM-10% solution. In brief, the power density of incident light is quantified by employing a cuvette containing pure water and a mixed solution, and the resulting discrepancy is multiplied by the area of light irradiation to determine the absorbed energy (I_{in}). The hs value is calculated from the temperature decay curve after the light was turned off. For the hs value, the time constant (τ_s) of solution heat transfer should be introduced as the Eq. (S3):

$$\tau_s = \frac{mC}{hs} \quad \text{(S3)}$$

The time constant (τ_s) is calculated according to the following the Eq. (S4):

$$ln\left(\frac{T_t - T_0}{T_{max} - T_0}\right) = \frac{-t}{\tau_s} \quad \text{(S4)}$$

6. Detailed information about FDTD simulation and computational details

The finite difference time domain (FDTD) method was employed to calculate the electric field distribution in WO_2@C/$Mn_{0.5}Cd_{0.5}S$ systems. Based on the characterization results of SEM and TEM, a simulation model of FDTD calculation was established. The boundary conditions in both x, y and z directions were set as perfectly matched layer to prevent unphysical scattering. In addition, the mesh of the whole simulation region is perfectly divided into 0.1 nm, which ensures the acquisition of accurate calculation results. Importantly, A full-field scattered field light source is used as the excitation light, which is vertically incident on the surface of the nanostructure along the z direction. And the electric field distribution of the nanostructures in the x-y and x-z planes was obtain by an electric field monitor, respectively.

The density functional theory (DFT) calculations were carried out by using the Vienna ab initio Simulation Package (VASP)[4]. The structures were optimized by considering the model of WO_2@C (011)/ $Mn_{0.5}Cd_{0.5}S$ (002) according to the HRTEM and XRD results. Perdew-BurkeErnzerhof (PBE) method based on the generalized gradient approximation (GGA) was adopted to analyze the properties of the material. The cutoff energy for plane wave truncation was selected as 500 eV. The first Brillouin zone uses a 3 × 3 × 1 Monkhorst-Pack (MP) grid for sampling. The interaction between ions and electrons was investigated using the projected augmented wave (PAW) method. The structure optimization process was terminated until the force on each atom was less than 0.02 eV/Å and the energy change was less than 1×10^{-5} eV. The DFT-D3 semi-empirical correction proposed by Grimme was included in the calculation to obtain the correct structure. The hydrogen adsorption energy (ΔE_H) was calculated from DFT total energies. For reference, the Gibbs free energy of adsorption (ΔG_H) can be obtained from ΔE_H* by incorporating vibrational zero-point energy and entropy corrections: ΔG_H* = ΔE_H* + ΔZPE – TΔS..

$$\Delta G\_H^* = \Delta E\_H^* + \Delta ZPE - T\Delta S. \quad \text{(S5)}$$

where ΔE and ΔZPE represent the calculated adsorption energy and the zero-point energy correction, respectively. T is the temperature. ΔS is the entropy change.

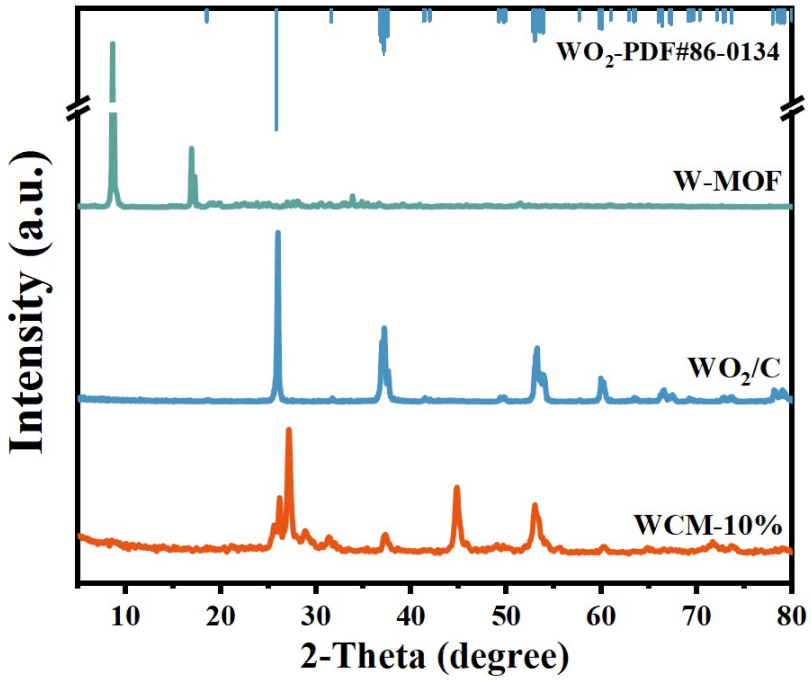

Fig. S1 The XRD patterns of W-MOF, WO_2@C and WCM-10%.

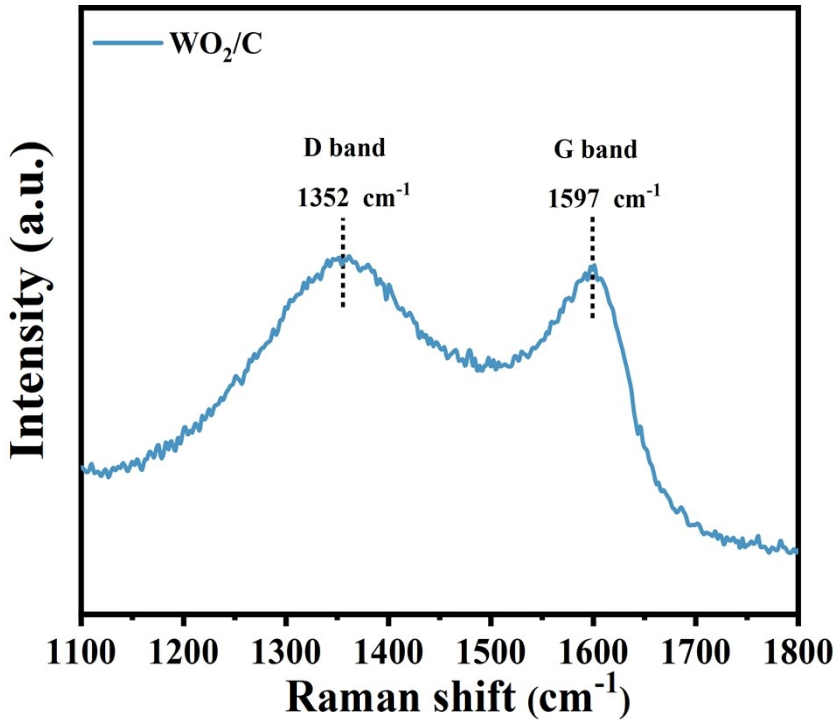

Fig. S2 Raman spectrum in the range of 1100 to 1800 cm^{-1}.

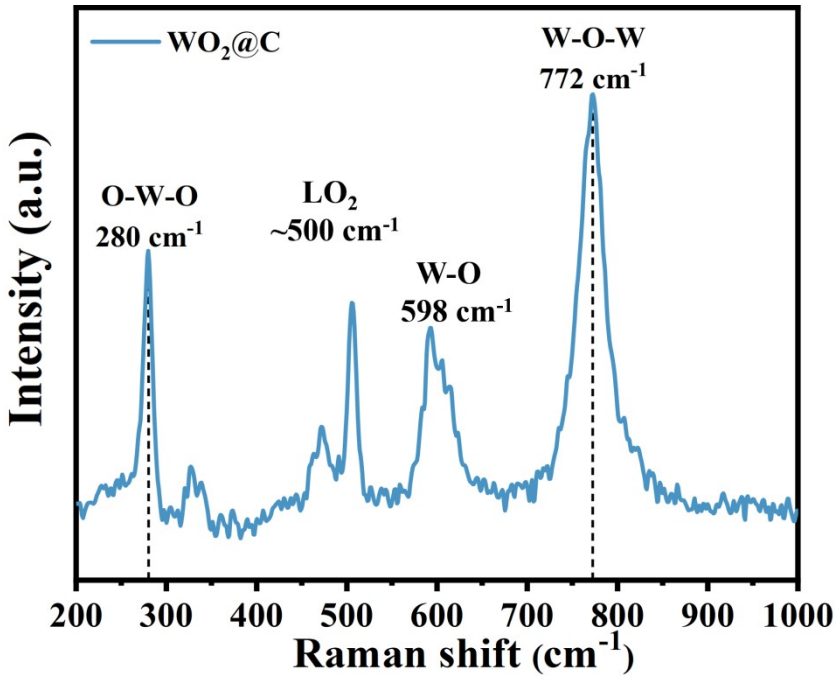

Fig. S3 Raman spectrum in the range of 200 to 1000 cm^{-1}.

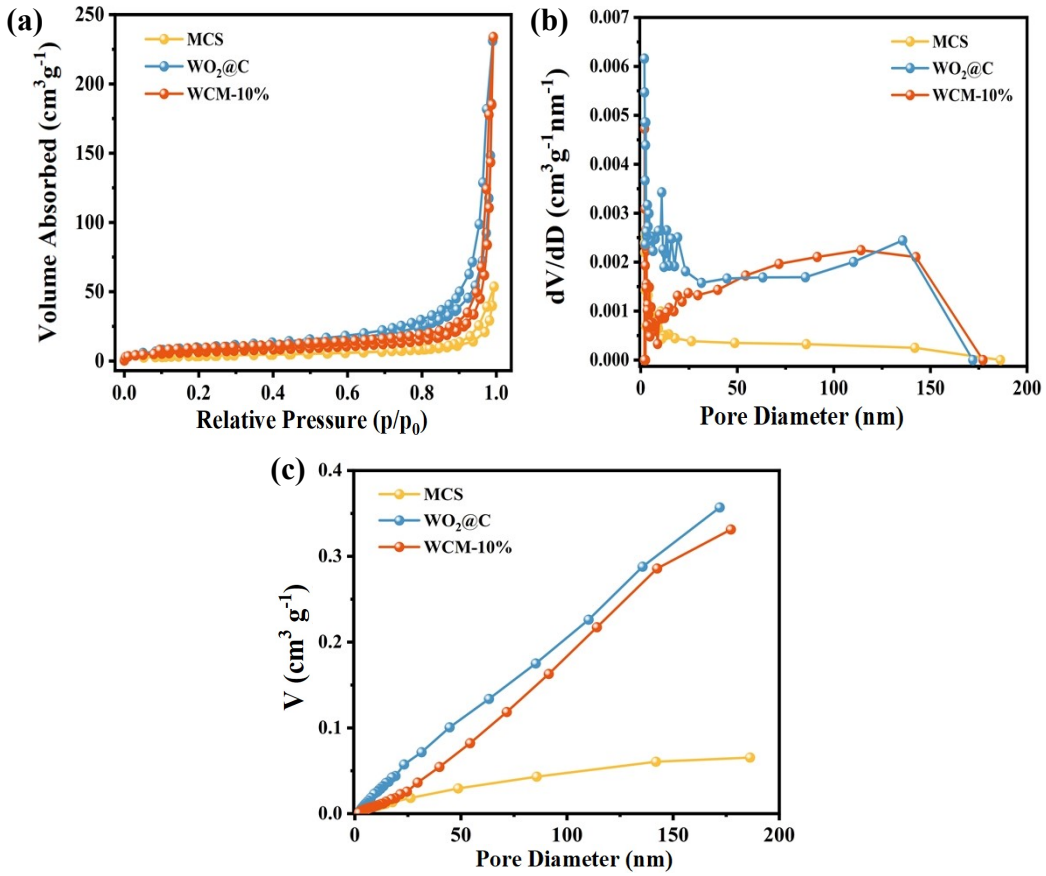

Fig. S4 (a) N_2 adsorption-desorption isotherms, (b) pore size distributions diagram, and (c) the Pore volume of of MCS, WO_2@C and WCM-10%.

Table S1 Summary of textural properties of MCS, WO_2@C and WCM-10%.

Sample	Surface area ($m^2 g^{-1}$)	Mean pore diameter (nm)	Pore volume ($cm^3 g^{-1}$)
MCS	13.02	18.06	0.07
WO_2@C	34.11	29.73	0.36
WCM-10%	23.65	43.23	0.33

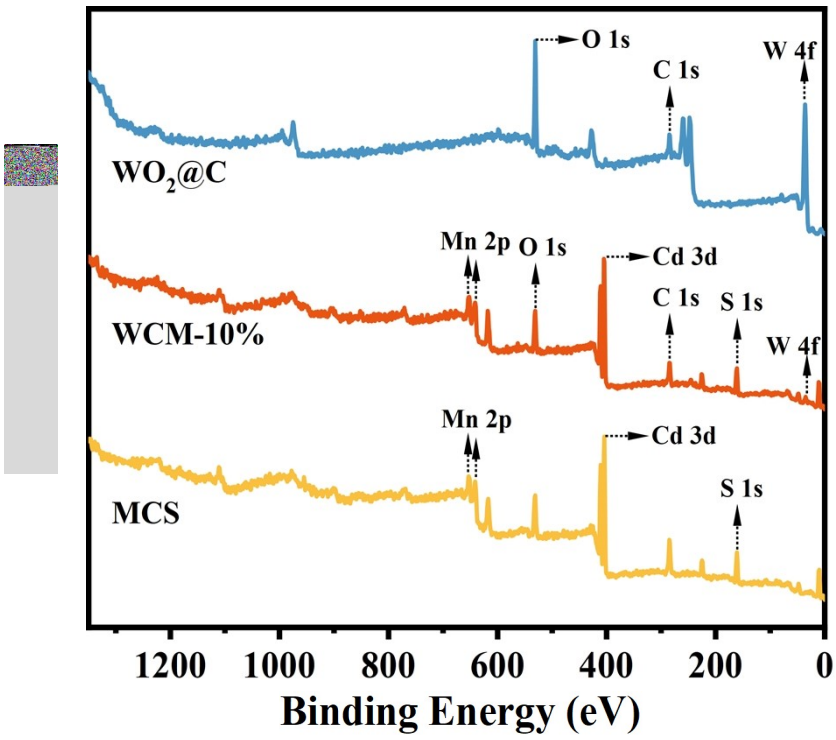

Fig. S5 XPS spectra of full survey of WO_2@C, WCM-10% and MCS photocatalyst.

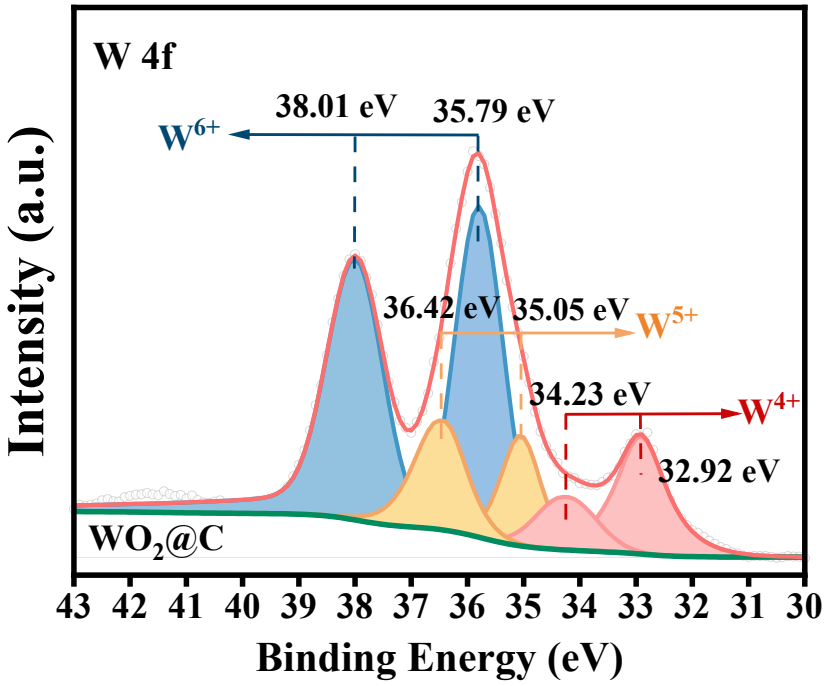

Fig. S6 High resolution XPS spectra of W 4f of WO_2@C.

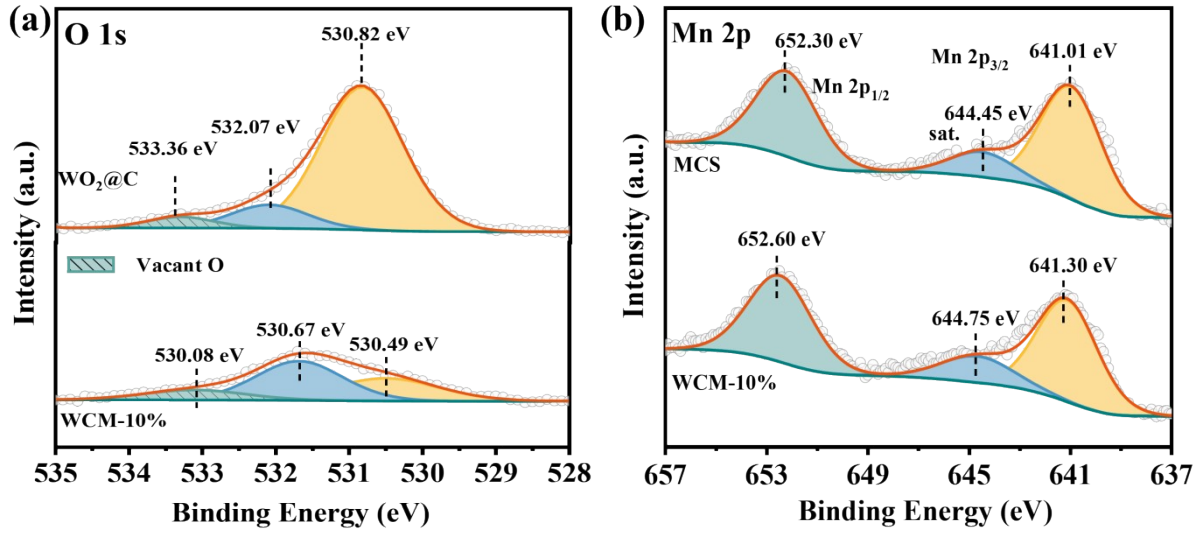

Fig. S7 High resolution XPS spectra of (a) O 1s of WO_2@C and WCM-10% and (b) Mn 2p of MCS and WCM-10%.

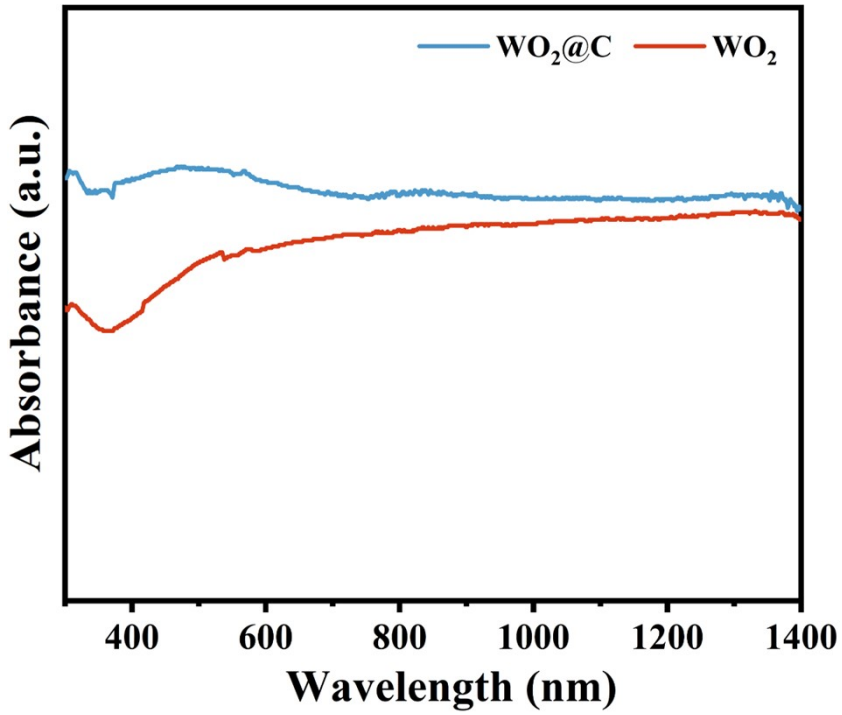

Fig. S8 UV-vis absorption spectra of WO_2@C and pure WO_2.

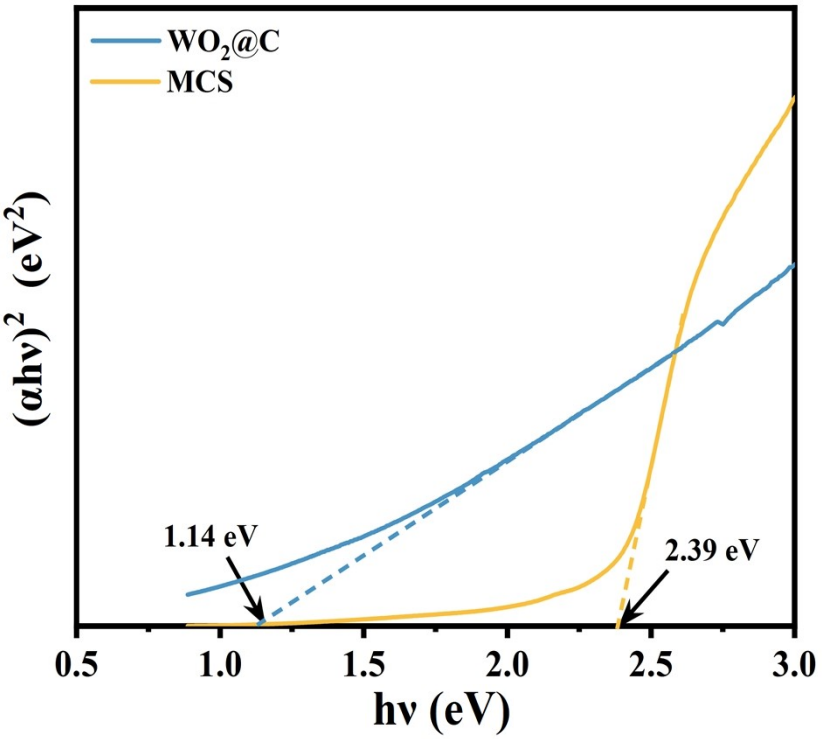

Fig. S9 Band gap spectra of WO_2@C and MCS.

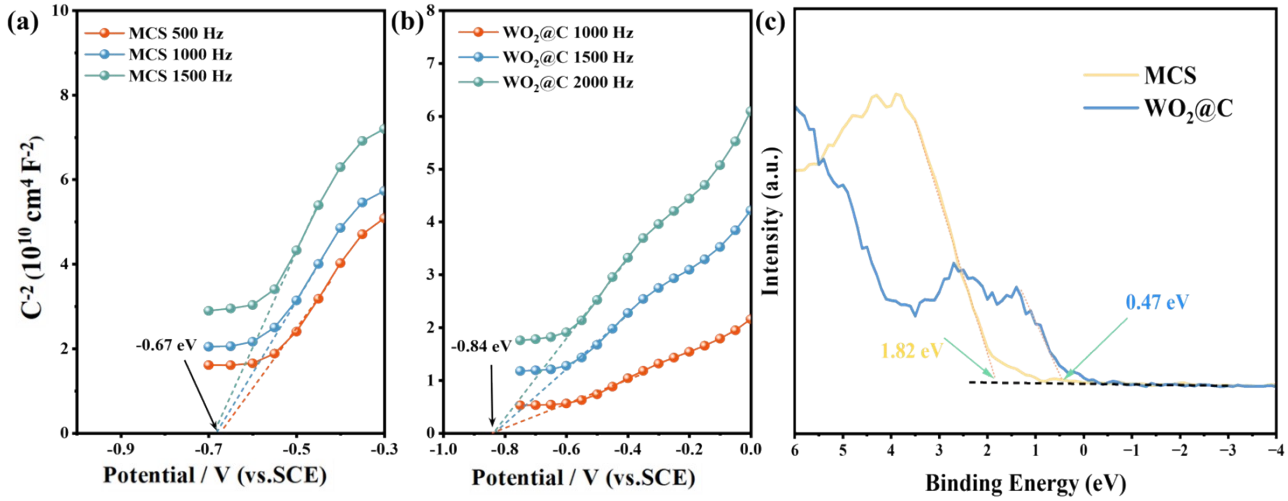

Fig. S10 The Mott–Schottky plots of (a) MCS and (b) WO_2@C under three different frequencies.(c) VB XPS spectra of MCS and WO_2@C.

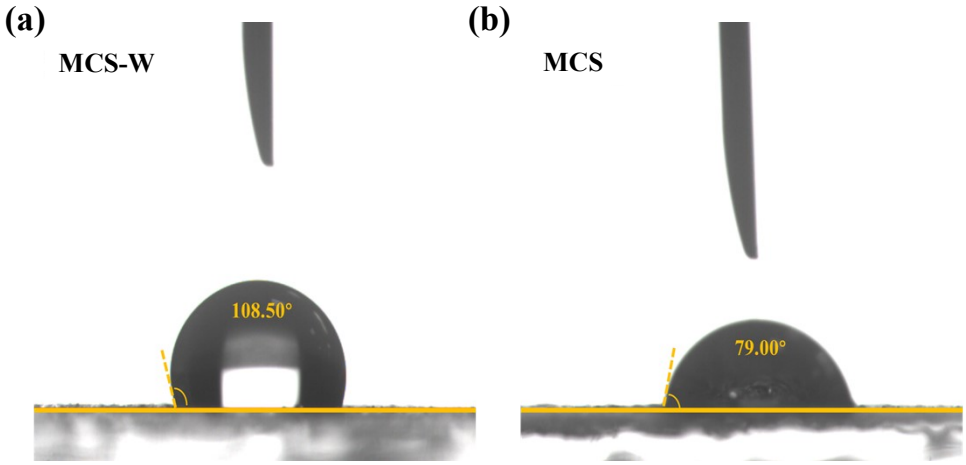

Fig. S11 Water contact angle of MCS-W and MCS synthesized with different solvents, respectively, (a) in water, and (b) in TEG.

For comparison, another $Mn_{0.5}Cd_{0.5}S$ crystallite was prepared by an alternative hydrothermal method. The similar experimental procedure was used except that the water was adopted as the solvent. The obtained $Mn_{0.5}Cd_{0.5}S$ was denoted as MCS-W. The high hydrogen release rate may also be attributed to the high affinity for water, as evidenced by the water contact Angle feature photo in Fig. S11.

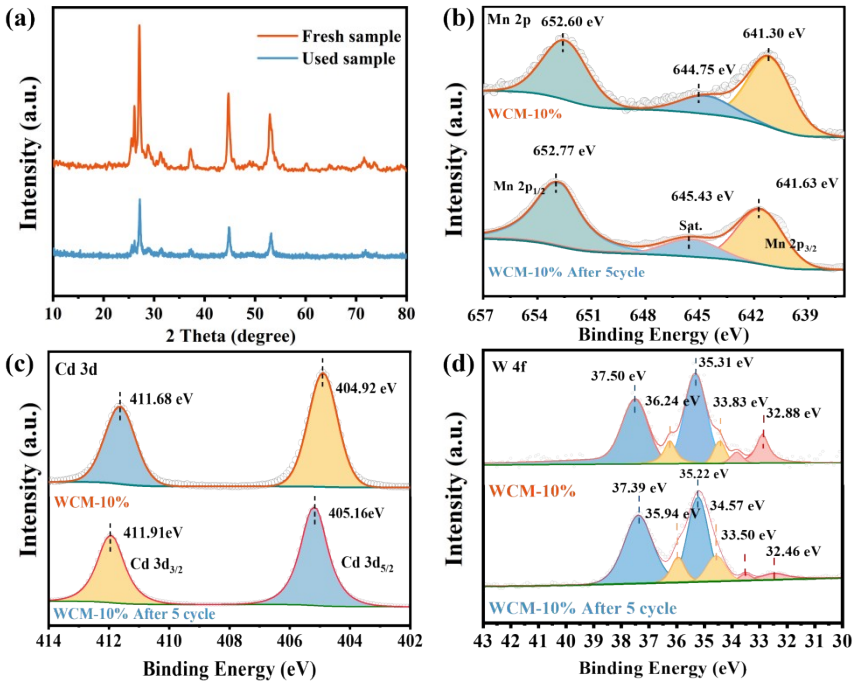

Fig. S12 (a) The XRD patterns and (b-d) high resolution XPS spectra of Mn 2p, Cd 3d and W 4f of fresh and used WCM-10% photocatalyst.

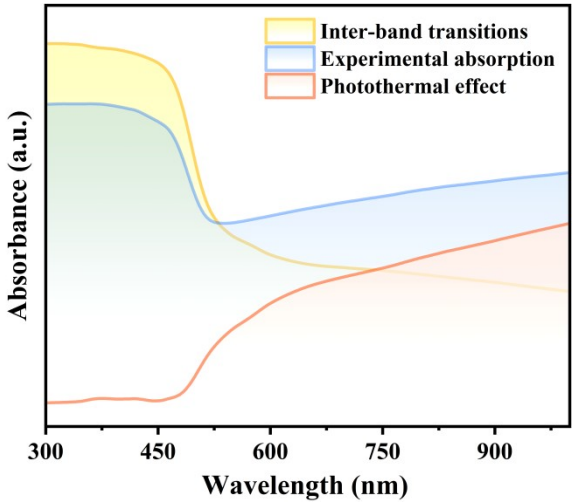

Fig. S13 Contribution of inter-band excitation and photothermal effect

Table S2 Comparison of photocatalytic overall water splitting performance in similar systems

Catalyst	Wavelength	H_2 production	AQE	Ref.
WO_2@C/$MnC_{0.5}d_{0.5}S$	AM 1.5G	234.1 μmol g^{-1} h^{-1}	1.94 % (420 nm)	This work
CoTCPPOMe/P-MCS	420 nm LED	2.1 μmol h^{-1}	—	5
SiQDs/Cu-doped $ZnIn_2S_4$	λ ≥ 420 nm	210 μmol g^{-1} h^{-1}	2.57 % (420 nm)	6
Pt@CrO_x-CdS/WPCN	AM 1.5G	11.94μmol h^{-1}	—	7
$Co_{0.01}Mn_{0.29}Cd_{0.7}S$	λ ≥ 420 nm	443.12 μmol g^{-1} h^{-1}	4.08 % (420 nm)	8
$Nb_4C_3T_x$MXene@ZIS-OH	λ > 420 nm	53.7 μmol g^{-1} h^{-1}	1.2 % (380 nm)	9
CdS-IIP	AM 1.5G	69.84 μmol g^{-1} h^{-1}	0.19 % (420 nm)	10
ZIS-WO/C-wood	AM 1.5G	169.2 μmol g^{-1} h^{-1}	—	11
CdSe/PDI	λ > 380 nm	120.7 μmol g^{-1} h^{-1}	—	12
ZnCdS/PO/FeCoNiPi–MnO	λ ≥ 420 nm	0.29 mmol h^{-1}	1.29 % (420 nm)	13

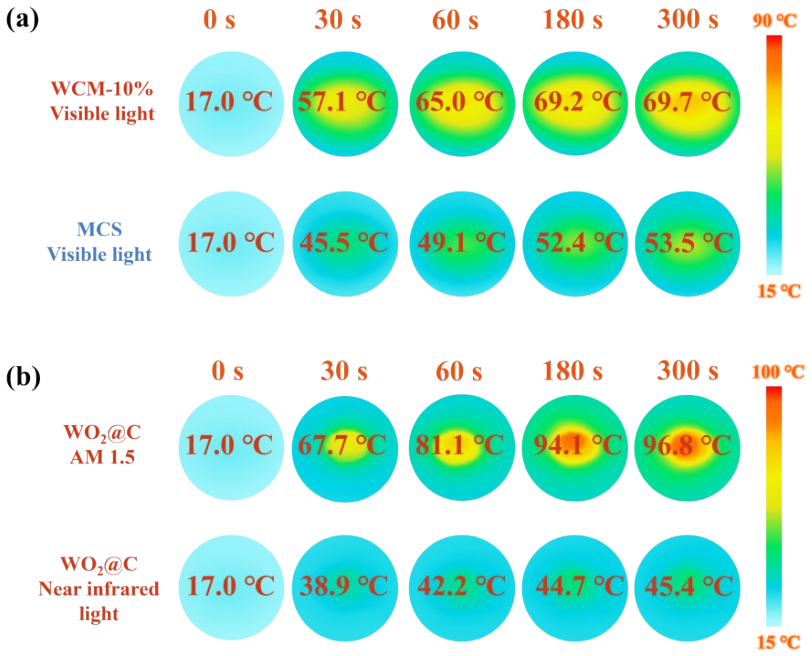

Fig. S14 The photothermal diagram of (a) MCS and WCM-10% under visible light and (b) WO_2@C under AM 1.5G simulated sunlight and NIR light

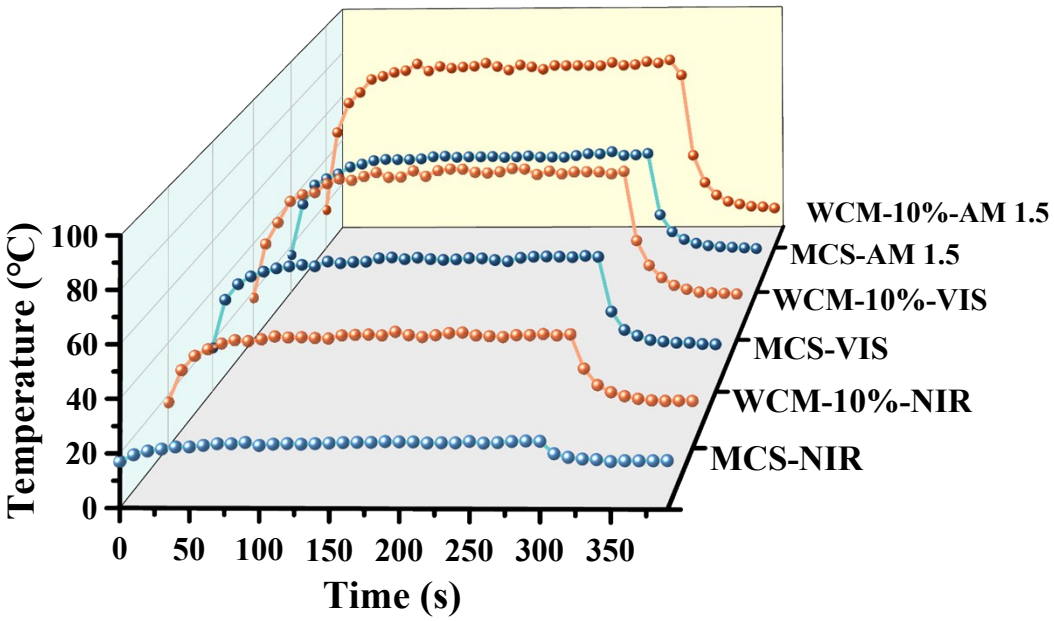

Fig. S15 The corresponding temperature change curves of MCS and WCM-10% after continuous irradiation with different light.

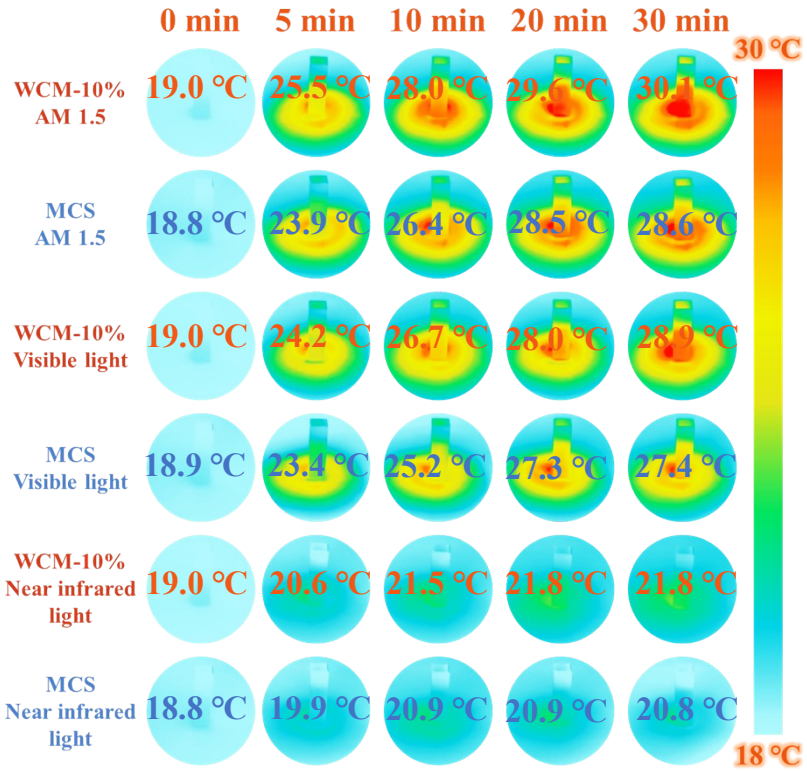

Fig. S16 The photothermal diagram of MCS and WCM-10% in an aqueous system after continuous irradiation with different light.

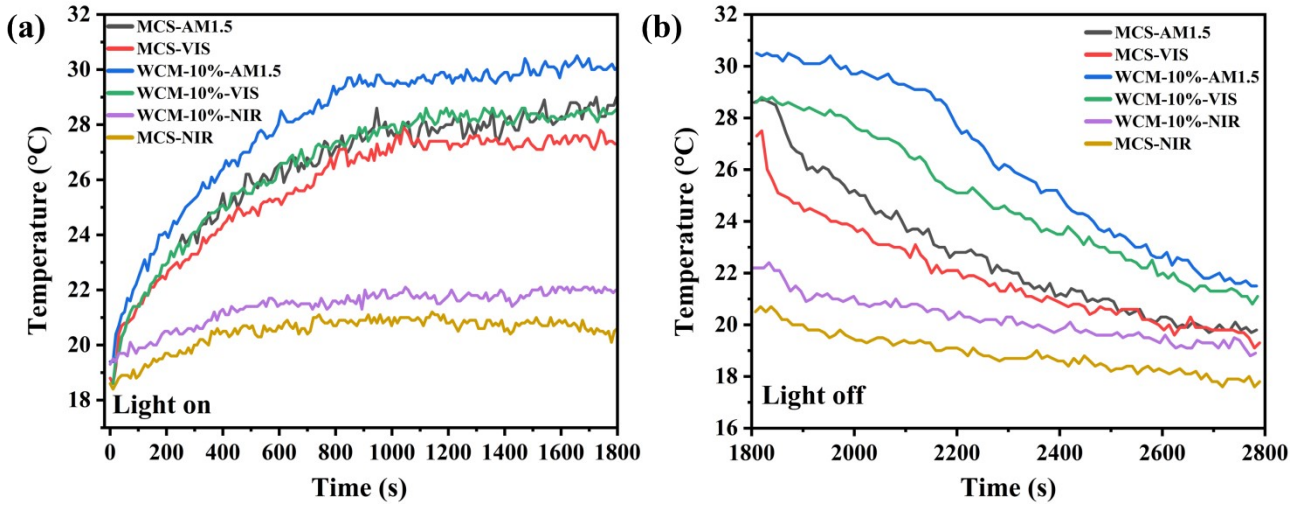

Fig. S17 The corresponding temperature change curves of MCS and WCM-10% solution after continuous irradiation with different light: (a) Heating curves and (b) Cooling curves.

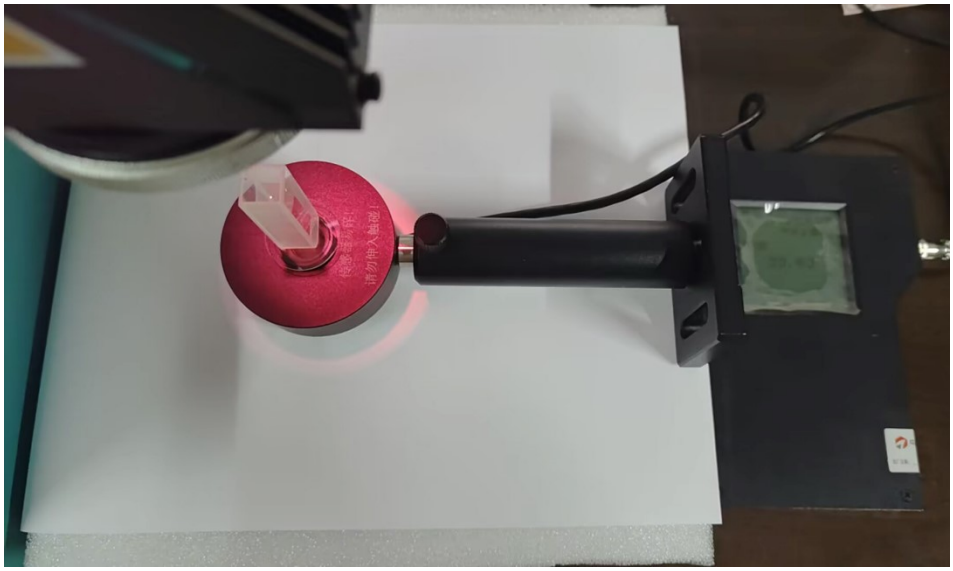

Fig. S18 The experimental apparatus for measuring the optical power and power density of water and mixed solutions.

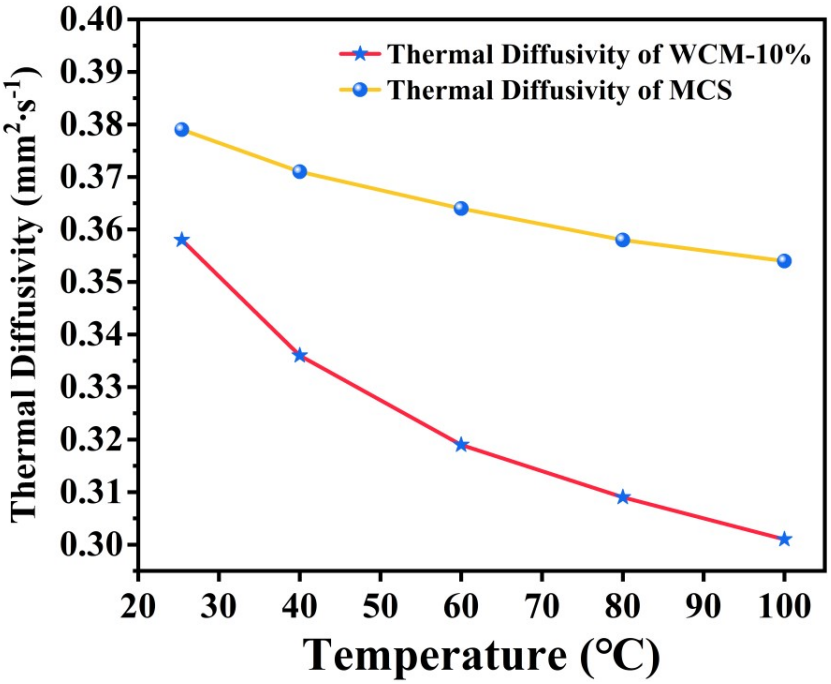

Fig. S19 Thermal diffusivity of WCM-10% and MCS

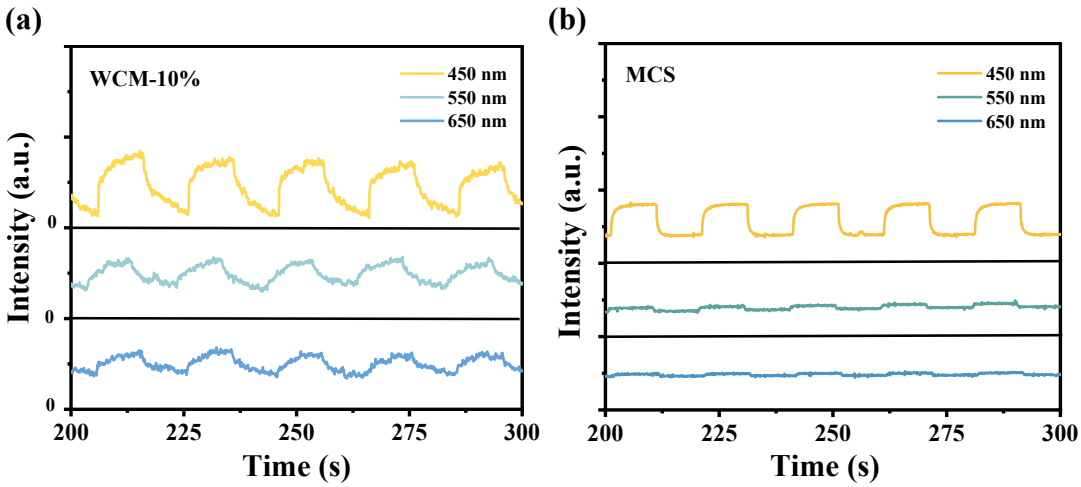

Fig. S20 (a and b) The wavelength-dependent photocurrent test in the MCS and WCM-10% samples at 450 nm, 550 nm and 650 nm.

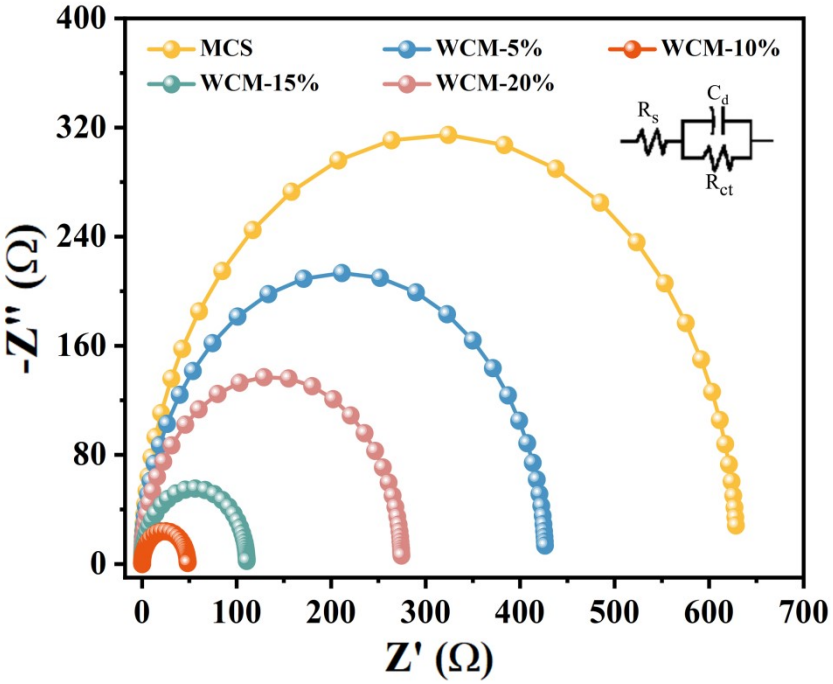

Fig. S21 The EIS Nyquist plots of MCS and WCM-X%.

Table S3 The time-resolved PL decay lifetime of MCS and WCM-10%.

	τ_1 (ns)	A_1 (%)	τ_2 (ns)	A_2 (%)	τ (ns)
MCS	1.49	5.40	49.57	94.60	46.97
WCM-10%	2.21	2.09	97.16	97.91	95.18

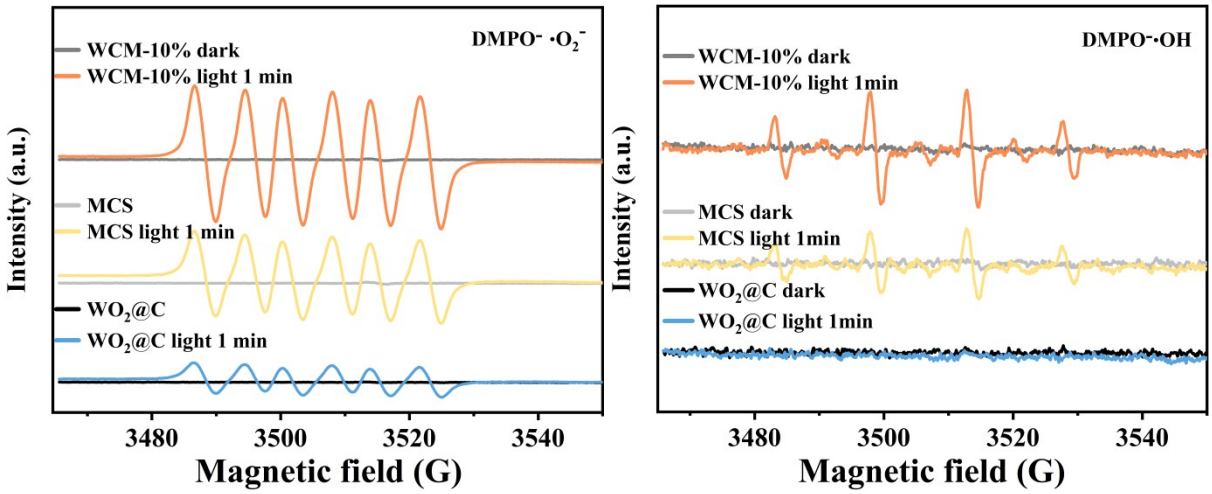

Fig. S22 In-situ ESR signals of (a) DMPO-·O^{2-} and (b) DMPO-·OH radical for MCS, WO_2@C, and WCM-10% samples under AM1.5 light irradiation.

Table S4 Bader charge analysis of WCM

Component	△q (e)
$Mn_{0.5}Cd_{0.5}S$	-0.115059 e
WO_2	0.116392 e
C	-0.001208 e

References

1 K. Qian, L. Du, X. Zhu, S. Liang, S. Chen, H. Kobayashi, X. Yan, M. Xu, Y. Dai, R. Li, *J. Mater. Chem. A*, 2019, **7**, 14592-14601.

2 W. Shi, Z. Chen, J. Lu, X. Sun, Z. Wang, Y. Yan, F. Guo, L. Chen, G. Wang, *Chem. Eng. J.*, 2023, **474**, 145690.

3 F. Kresse, *Phys. Soc. B*, 1996, 54, 11169.

4 N.T. Nhat Hang, N. Van Canh, N.H. Hoa, P.D. Du, P.H. Le, V. Nguyen, *Carbon*, 2022, **199**, 462-468.

5 X. Yang, W. Sun, B. Li, Y. Dong, X. Huang, C. Hu, M. Chen, Y. Li, Y. Ding, *J. Colloid Interface Sci.*, 2024, **655**, 779-788.

6 W. Shi, B. Ge, P. Jiang, Q. Wang, L. He, C. Huang, *Appl. Catal., B*, 2024, **354**, 124121.

7 H. Li, F. Yu, A. Li, Q. Deng, W. Hu, W. Hou, *Chem. Eng. J.*, 2024, **489**, 151219.

8 W. Tang, T. Zeng, L. Zhang, B. Li, G. Wang, X. Xing, Y. Ding, C. Hou, W. Dong, *Chem. Eng. J.*, 2023, **470**, 143898.

9 X. Liu, J. Zhang, J. Xu, Y. Li, Y. Du, Y. Jiang, K. Lin, *J. Colloid Interface Sci.*, 2023, **633**, 992-1001.

10 Q. Zhang, W. Luo, T. Yang, R. Li, Q. Gao, X. Cai, S. Zhang, Y. Fang, X. Zhou, F. Peng, S. Yang, *Sep. Purif. Technol.*, 2024, **346**, 127391.

11 Y. Wang, W. Huang, S. Guo, X. Xin, Y. Zhang, P. Guo, S. Tang, X. Li, *Adv. Energy Mater.*, 2021, **11**, 2102452.

12 J. Xue, C. Lei, Q. Li, Z. Sun, H. Li, S. Ding, H. Jia, Q. Shen, X. Liu, Y. Zhu, *J. Mater. Chem. A*, 2024, **12**, 6582-6591.

13 J. Song, H. Su, M. Fang, L. Han, J. Chu, C. Li, R. Miao, W. Yao, G. Zhang, A. You, *J. Mater. Chem. A*, 2022, **10**, 16029-16036.